Highly Stable Fe^{2+}/Ti^{3+}-Based Fluoride Cathode Enabling Low-Cost and High-Performance Na-Ion Batteries

Jungmin Kang, Jinho Ahn, Hyunyoung Park, Wonseok Ko, Yongseok Lee, Seokjin Lee, Sangyeop Lee, Sung-Kyun Jung,* and Jongsoon Kim*

Grid-scale energy storage system is the need of batteries with low-cost, high-energy-density, and long cycle life. The requirement promotes the discovery of cathode materials enabling the storage of charge carrier ion within the open framework crystal structure having multi-dimensional diffusion path exhibiting small volume change. Herein, Na_2TiFeF_7 is reported as a promising fluoride-based cathode material for sodium-ion batteries (SIBs). Through combined studies using various experiments and first-principles calculations, it is confirmed that Na_2TiFeF_7 with 3D diffusion pathway delivers a specific capacity of ≈185 mAh g^{-1} at C/20 with an average operation voltage of ≈3.37 V (vs Na^+/Na) including the high $Fe^{2+/3+}$ redox potential (≈3.75 V). Even at 5C, a specific capacity of ≈136 mAh g^{-1} is retained (≈73% of its theoretical capacity) owing to the low band gap energy (≈1.83 eV) and the low activation barrier energies (≈477.68 meV) required for facile Na^+ diffusion, indicating the excellent power-capability. Moreover, Na_2TiFeF_7 composed of three-dimensionally interconnected $(Fe, Ti)F_6$ octahedra delivers an outstanding capacity retention of ≈71% after 600 cycles at 1 C owing to the small structural volume change (≈0.96%) during Na^+ de/intercalation. These findings provide insight into the development of fluoride-based novel cathode materials for high-performance SIBs.

1. Introduction

The application of rechargeable batteries to grid-scale energy storage systems is needed for efficient usage of eco-friendly generated energies.[1,2] Recently, sodium-ion batteries (SIBs) have been regarded as suitable for grid-scale applications because of their cost-effectiveness resulting from the use of earth-abundant resources. Intensive research has been underway on earth-abundant element-based layered oxides, Na_xMO_2 (M = Fe, Mn, etc.), with low production cost and inherently large theoretical gravimetric capacities as promising cathode materials for SIBs.[3–6]

Due to the large ionic radius of Na^+ ion, bond ionicity with oxygen, and repulsion between oxygen slabs as vacancy concentration,[7,8] two types of polymorphs have been developed as a function of Na contents in layered structure (O-type for x ~ 1 and P-type for $0.4 < x < 0.7$).[9,10] Despite its large theoretical capacity of above 200 mAh g^{-1}, however, O3-type $NaFeO_2$ only delivers a small specific capacity of ≈100 mAh g^{-1} because of the instability of the Fe^{3+}/Fe^{4+} redox reaction.[11,12] This low specific capacity can be overcome by introducing Mn at TM sites and vacancies at Na sites together ($Na_xFe_{1-y}Mn_yO_2$) to form a P2-type layered oxide, resulting in a large specific capacity of ≈200 mAh g^{-1}.[13] However, the presence of Mn^{3+} in the structure leads to structural instability due to Jahn–Teller distortion, resulting in poor cyclability and power-capability.[14] Furthermore, relative low energy density of SIBs compared to LIBs due to the low redox potential (≈3 V vs Na^+/Na) is still remained as critical issue to be overcome for application to substitute currently being used LIBs.[15]

As one of the strategies to increase the redox potential, inductive effect induced by polyanion groups such as $(PO_4)^{3-}$, $(SO_4)^{2-}$, etc. has been widely applied for development of high-voltage cathode materials. It was also reported that polyanion-based cathode materials for SIBs can deliver outstanding cyclability owing to high structural stability.[16–18] However, the application of polyanions inevitably results in the lowered gravimetric energy density compared to the layered-type oxide cathodes, because of the increased molar mass. Thus, the trade-off between available capacity and structural stability must be considered in the development of novel cathode materials for SIBs.

Among the numerous cathode materials for Na-ion batteries, fluoride materials have potential to be promising candidate for cathode by taking both merits of layered-oxide and polyanion cathode materials such as large gravimetric capacity and high

J. Kang, J. Ahn, H. Park, W. Ko, Y. Lee, S. Lee, S. Lee, J. Kim
Department of Energy Science
Sungkyunkwan University
Suwon 16419, Republic of Korea
E-mail: jongsoonkim@skku.edu
J. Kang, J. Ahn, H. Park, W. Ko, Y. Lee, S. Lee, S. Lee, J. Kim
SKKU Institute of Energy Science and Technology (SIEST)
Sungkyunkwan University
Suwon 16419, Republic of Korea
S.-K. Jung
Department of Energy Engineering
School of Energy and Chemical Engineering
Ulsan National Institute of Science and Technology (UNIST)
Ulsan 44919, Republic of Korea
E-mail: skjung@unist.ac.kr

operation voltage. The lighter weight of the fluoride ion compared with that of polyanion units is beneficial for achieving a high specific capacity. Furthermore, the fluorine ions in the structure enable a higher redox potential of transition-metal ions than oxygen ions through the inductive effect by the highest electronegativity.[19,20] However, development of fluoride-based cathode material has been limited to a small number of candidates such as $NaFeF_3$ or $KFeF_3$ derivatives so far, and energy density is still incompetent compared to other existing Na cathodes.[21–24] Even, some of fluoride-based cathodes require presodiation to fully utilize available high capacity.[25] But, the common issue of fluoride-based cathode materials generally suffer is poor reaction kinetics because of their large band-gap energies and low electronic conductivities,[26] resulting in drastic capacity fading at high rate of charging of fluoride-based cathode materials.

In this work, we investigated a novel Fe^{2+}/Ti^{3+}-based fluoride with a three-dimensional framework, Na_2TiFeF_7, as a promising cathode for SIBs. The presence of Ti^{3+} and Fe^{2+} ions in the Na_2TiFeF_7 structure enables the use of both the Ti^{3+}/Ti^{4+} and Fe^{2+}/Fe^{3+} redox reactions for a reversible ≈1.95 mol Na^+ ion de/intercalation, which corresponds to a specific capacity of ≈185 mAh g^{-1} at C/20 (1C = 189 mA g^{-1}). Na_2TiFeF_7 also exhibited a high-average operation voltage of ≈3.37 V (vs Na^+/Na) owing to the high theoretical Fe^{2+}/Fe^{3+} redox potential of ≈3.75 V, which is much higher than other Na-layered oxide cathode materials with the practical capacity of above 160 mAh g^{-1}.[27] Through first-principles calculation, it was demonstrated that the band-gap energy of Na_2TiFeF_7 (≈1.83 eV) is lower than that of other Fe-based fluoride materials and similar to that of the Fe-based oxide material, which implies that Na_2TiFeF_7 can exhibit higher electronic conductivity compared to other Fe-based fluoride materials. Furthermore, we confirmed that the theoretical activation barrier energy is sufficiently low (≈477.68 meV) for facile Na^+ diffusion in the structure of Na_2TiFeF_7, that can boost up the power-capability. Thus, even at 5C, ≈73% of the specific capacity of Na_2TiFeF_7 was retained, indicating the outstanding power-capability of Na_2TiFeF_7. Furthermore, after 600 cycles at 1C, Na_2TiFeF_7 exhibited a capacity retention of ≈71% compared with the initial capacity with a high coulombic efficiency of over 99%. This excellent capacity retention was achieved because of the small volume change (≈0.96%) during charge/discharge resulting from the high structural stability by the three-dimensionally interconnected $(Fe, Ti)F_6$ octahedra, which is clearly distinguished from the large structural change of general layered oxide cathodes with the two-dimensional framework. Our findings will broaden the boundaries of fluoride-based cathode materials and provide intuition for developing SIBs with high-energy density and low-cost.

2. Results and Discussion

2.1. Structural and Morphological Properties of Na_2TiFeF_7

The crystal structure of the synthesized Na_2TiFeF_7 was confirmed through the Rietveld refinement of the XRD data (**Figure 1**a). A pure phase of the trigonal structure belonging to the $P3_121$ space group was successfully prepared without any impurities or second phases. The lattice parameters were calculated to be $a = b = 7.42091(9)$ Å and $c = 18.2752(4)$ Å with low values of the reliability factors ($R_P = 2.85\%$, $R_I = 3.76\%$, $R_F = 1.96\%$, and $\chi^2 = 2.15\%$), indicating the high reliability of the Rietveld refinement results. Detailed structure information, including the atomic positions, B_{iso} values, and occupancies, is provided in Table S1 (Supporting Information). Transmission electron microscopy (TEM) and energy-dispersive X-ray spectroscopy (EDS) analyses revealed that the elements of Na, Ti, Fe, and F were homogeneously distributed in the Na_2TiFeF_7 particles (Figure 1b) and that the total elemental ratio of Na, Ti, and Fe of the Na_2TiFeF_7 particle was approximately 2.00:0.99:1.01, which was in good agreement with the inductively coupled plasma atomic emission spectroscopy (ICP-AES) analysis (Table S2, Supporting Information). The average particle size of Na_2TiFeF_7 was confirmed to be 400 nm through scanning electron microscopy (SEM), which is consistent with the TEM analysis in Figure 1b and Figure S1 (Supporting Information).

Based on the structure information obtained from the Rietveld refinement and XRD analyses, bond-valence energy landscape (BVEL) analysis on Na_2TiFeF_7 was performed using the *Bond_str* program in the FullProf package,[28] to identify the visualized crystal structure and the possible Na^+ diffusion pathways in the structure (Figure 1c–d). In the crystal structure of Na_2TiFeF_7, all the $(Fe, Ti)F_6$ octahedra were three-dimensionally interconnected with each other, indicating the high structural stability of Na_2TiFeF_7, and it was also confirmed that there are large three-dimensional pathways for facile Na^+ diffusion in the crystal structure of Na_2TiFeF_7. In addition, X-ray absorption nearest edge spectroscopy (XANES) analyses (Figure 1e–f) indicated that the average oxidation states of Fe and Ti ions in the Na_2TiFeF_7 phase are believed to be +2 and +3, respectively, by comparing white line energy with FeO and Ti_2O_3, which implies that Na ions in the structure can be reversibly de/intercalated through Fe^{2+}/Fe^{3+} and Ti^{3+}/Ti^{4+} redox reactions between $Na_2Ti^{(3+)}Fe^{(2+)}F_7$ and $Na_0Ti^{(4+)}Fe^{(3+)}F_7$ phases.

2.2. Theoretical Properties of Na_2TiFeF_7 for High Power-Capability

To verify the intrinsic electronic conductivity of Na_2TiFeF_7, we performed first-principles calculations on the band-gap energies of Na_2TiFeF_7 and various Fe-based fluoride and oxide materials. As shown in **Figure 2**a, Na_2TiFeF_7 was predicted to exhibit a band-gap energy of ≈1.83 eV, which is contributed by the partial density of state of Ti 3d. It is lower than not only that of various Fe-based fluoride materials (with values above ≈2.9 eV) but also that of $NaFeO_2$ (≈2.05 eV). Moreover, the dark brown color of the synthesized Na_2TiFeF_7 powder also indirectly supports a lower band-gap energy than that of FeF_2 (beige) or FeF_3 (pale green) (Figure S2, Supporting Information).

In addition, the theoretical activation barrier energies for Na^+ diffusion pathways in the crystal structure of Na_2TiFeF_7 were predicted using the nudged elastic band (NEB) method based on the first-principles calculation (Figure 2b–c). The predicted diffusion pathway mediated by the Na2 site is shown as the Na1–Na2–Na3 diffusion path, and it is consistent with the BVEL map exhibiting the possible positions of the Na^+ ion
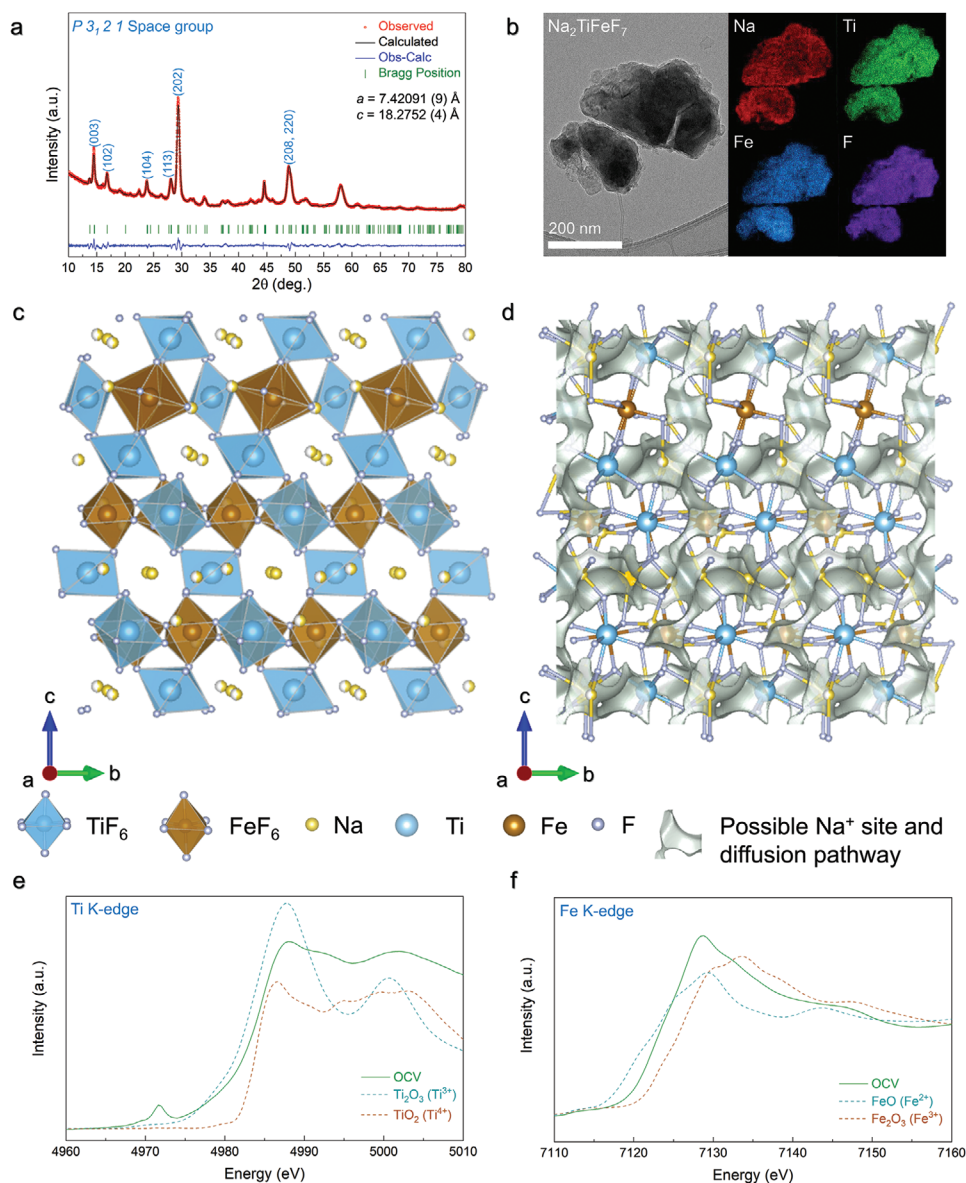
Figure 1. Structural, morphological characterization, and redox reaction of Na_2TiFeF_7. a) Refined XRD pattern of Na_2TiFeF_7. b) TEM image of Na_2TiFeF_7 and corresponding EDS mappings of Na, Ti, Fe, and F elements. c) Crystal structure of Na_2TiFeF_7. d) Three-dimensional (bc plane) BVEL analyses of Na_2TiFeF_7 with all possible Na^+ diffusion pathways in the crystal structure. e) Ti K-edge and f) Fe K-edge XANES analyses of Na_2TiFeF_7.

(Figure 1d). The activation barrier energies of the predicted three-dimensional diffusion pathways along Na1–Na2 and Na2–Na3 hopping were verified to be ≈305.13 and ≈477.68 meV, respectively, which indicate that the kinetics of Na^+ diffusion is mainly determined by diffusion from the Na2 to Na3 site and that the activation energy is sufficiently low for facile Na^+ diffusion within the structure. These first-principles calculation results on the band-gap and activation barrier energy for Na^+ diffusion indicate that Na_2TiFeF_7 can deliver outstanding power-capability as a promising cathode for SIBs.

The first-principles calculations were performed to predict and understand the theoretical redox potential and electronic configuration of Na_2TiFeF_7 during Na^+ de/intercalation. First, the formation energies of Na_xTiFeF_7 phases ($0 \leq x \leq 2$) were

calculated as Na^+/vacancy concentration and configuration using the cluster-assisted statistical mechanics (CASM) software to predict the redox potential. The convex-hull plot shows the overall formation energy of Na_xTiFeF_7 as a function of the vacancy concentration (Figure 2d). Then, the theoretical redox potentials of Na_xTiFeF_7 during Na^+ de/intercalation were calculated using the following equation:

$$V = -\frac{E[Na_{x_2}TiFeF_7] - E[Na_{x_1}TiFeF_7] - (x_2 - x_1)E[Na]}{(x_2 - x_1)F} \quad (1)$$

In this equation, V is the average redox potential in the range between each Na_xTiFeF_7 ($0 \leq x \leq 2$) composition, E is the theoretical formation energy of the most stable configuration
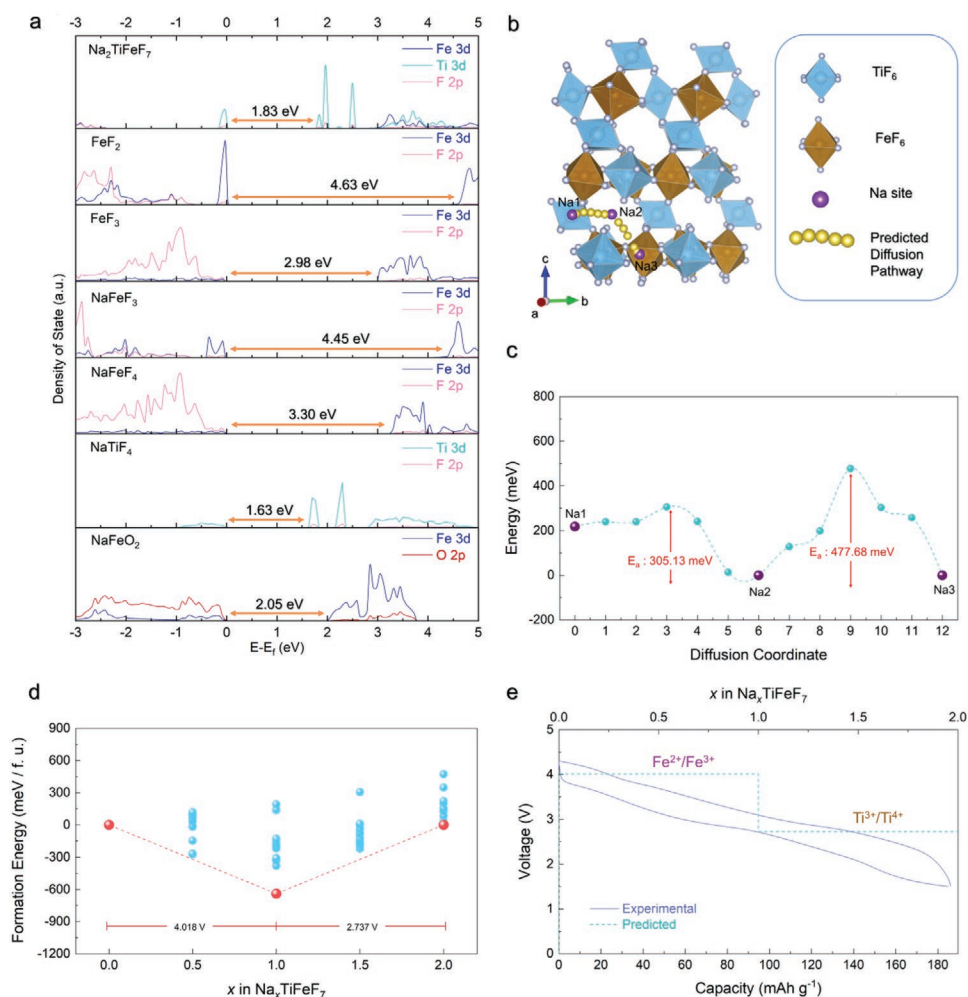
Figure 2. DFT calculation on band structure of Na_2TiFeF_7, prediction of possible Na^+ diffusion pathways and electrochemical performance. a) pDOS of Fe 3d and Ti 3d of various cathode materials for Na-ion batteries. b) Diffusion pathways for Na ion with c) energy landscape determined using the NEB method in Na_2TiFeF_7 structure. d) Convex-hull plot for various Na_xTiFeF_7 configurations ($0 \leq x \leq 2$) with theoretical redox potential. e) Comparison of predicted redox potential of Na_xTiFeF_7 and its experimentally measured charge/discharge curves for the cycle.

of each Na_xTiFeF_7 composition, and F is the Faraday constant. It was predicted that ≈2 mol Na^+ could be de/intercalated at 2.74 and 4.0 V (vs Na^+/Na), respectively. The theoretical redox potentials of Na_xTiFeF_7 were compared with the experimental charge/discharge profile of Na_2TiFeF_7 measured at C/20 (1C = 189 mA g^{-1}). It was demonstrated that the theoretically predicted redox potential of Na_xTiFeF_7 was well matched with the electrochemically tested de/intercalation profiles by allowing for slight over estimation, and the average operation voltage was confirmed to be ≈3.37 V (Figure 2e). To clarify the origin of both redox potentials (2.74 and 4.0 V), the integrated spin moments of Ti and Fe ions of Na_xTiFeF_7 of various compositions were theoretically predicted, as shown in Figure S3 (Supporting Information). Before extraction of Na ions from Na_2TiFeF_7, the total number of electron spins of Ti and Fe ions were confirmed to be 1 and 4, respectively, which correspond to Ti^{3+} and Fe^{2+}, given the electron configuration. At the initial charging of 1 mol Na^+ deintercalation from Na_2TiFeF_7 to Na_1TiFeF_7, the total number of electron spins of Ti ions was changed from +1 to 0, whereas the total number of electron

spins of Fe was maintained at 4. In addition, at the second step of charging from Na_1TiFeF_7 to Na_0TiFeF_7, the total spin number of Fe ions increased from 4 to 5 without a change in the total spin number of Ti. These results indicate that ≈2.0 mol Na^+ can be de/intercalated from Na_2TiFeF_7 in the order of Ti^{3+}/Ti^{4+} and Fe^{2+}/Fe^{3+} redox reactions corresponding to theoretically predicted 2.7 and 4.0 V. The experimentally observed ≈3.75 V value of the Fe^{2+}/Fe^{3+} redox reaction is comparable to the highest potential of 3.8 V from the alluaudite-type $Na_2Fe_2(SO_4)_3$ structure.[29] This result implies that fluoride-based intercalation-type compounds are worthy of exploration as high-voltage cathode materials beyond polyanion compounds.

2.3. Outstanding Electrochemical Properties of Na_2TiFeF_7 Under the SIB System

The power-capability of Na_2TiFeF_7 was measured in the voltage range of 1.5–4.3 V (1C = 189 mA g^{-1}) by varying the current density. Na_2TiFeF_7 delivered a large specific capacity

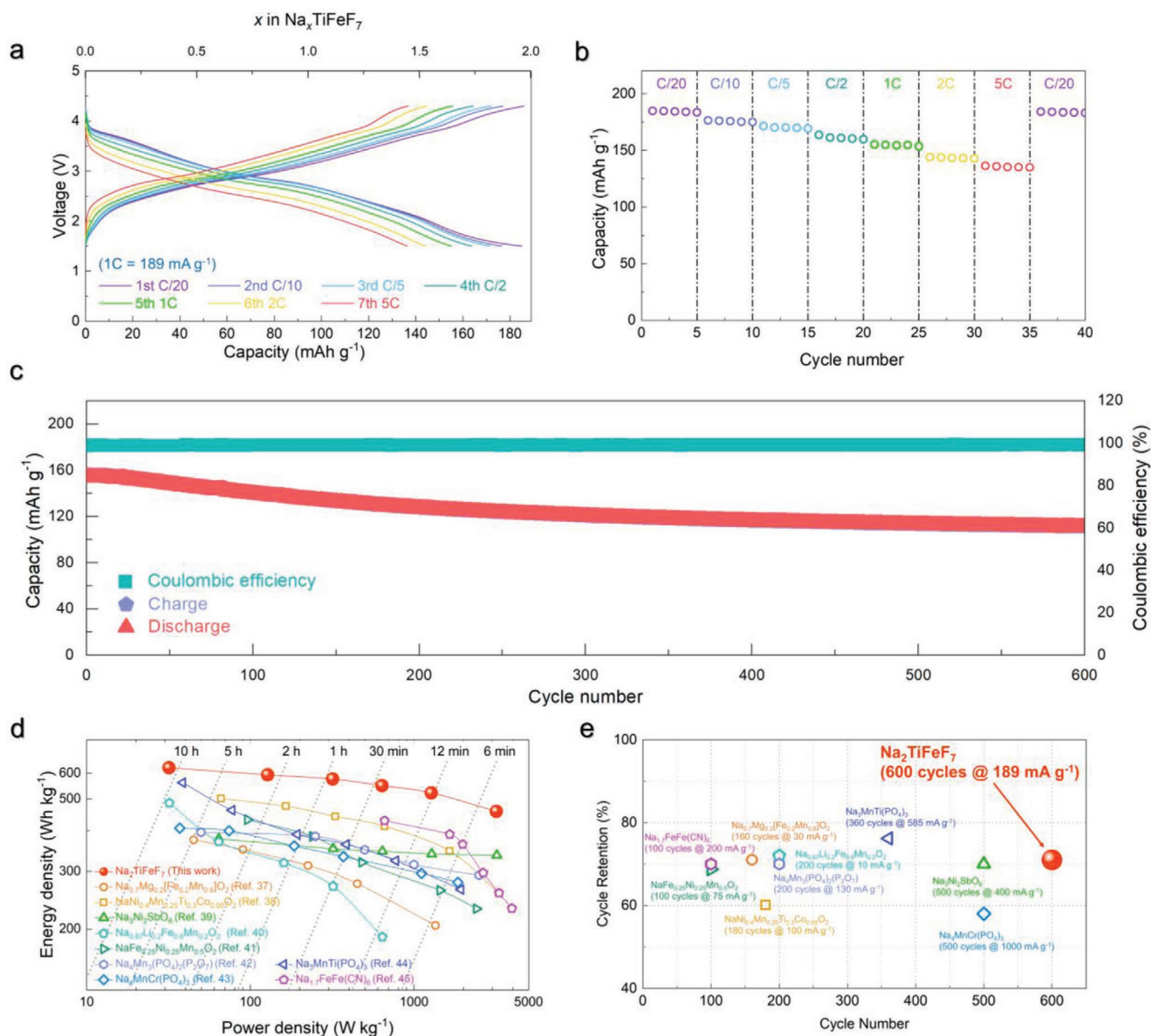**Figure 3.** Electrochemical performance of Na_2TiFeF_7 with high power and long-term cycle stability based on experiments. a) Charge/discharge profiles of Na_2TiFeF_7 in the range of 1.5–4.3 V at various current rates. b) Power-capability of Na_2TiFeF_7 with several cycles at various current rates. c) Cycle performance of Na_2TiFeF_7 at 1C over 600 cycles in the voltage range of 1.5–4.3 V (vs Na^+/Na). d) Comparison of energy and power densities among Na_2TiFeF_7 and other reported cathode materials for SIBs. e) Electrochemical properties of various cathode materials for SIBs.

of ≈185 mAh g^{-1} at C/20 with an average voltage of ≈3.37 V (vs Na^+/Na) (**Figure 3**a–b). In addition, Na_2TiFeF_7 exhibited outstanding power-capability by retaining a capacity of up to ≈136 mAh g^{-1} even at 5C, corresponding to ≈73% of the theoretical capacity. Moreover, it was confirmed that the Na_2TiFeF_7 electrode with 10 wt% conductive carbons exhibits similar power-capability to that with 20 wt% conductive carbons (Figure S4, Supporting Information), which implies that the outstanding power-capability of Na_2TiFeF_7 electrode mainly results from the Na_2TiFeF_7 itself rather than conductive carbon. This excellent capacity is due to the improved electronic conductivity resulting from the decrease of the bandgap energy (Figure 2a) and the three-dimensional diffusion

path for facile Na^+ ion diffusion with low activation energy barriers (Figure 2b–c). In addition, to measure the electronic conductivity, the DC polarization was conducted with an applied voltage of 1 V for 3000 s. As presented in Figure S5 (Supporting Information), it was verified that Na_2TiFeF_7 delivered the high electronic conductivity of ≈9.75 × 10^{-5} S cm^{-1}, which is much larger than the solid-electrolytes based on low electronic conductivity such as $Li_{6.4}La_3Zr_{1.4}Ta_{0.6}O_{12}$ (≈1.57 × 10^{-9} S cm^{-1}), $2LiCl–GaF_3$ (≈4 × 10^{-9} S cm^{-1}), etc.[30,31] As shown in Figure 3c, ≈71% of the initial specific capacity was retained after 600 cycles at 1C, with a high coulombic efficiency of above 99%. In addition, it was reported that the undesirable electrolyte decomposition can be occurred after numerous

cycles at the high voltage region.[32] Thus, the decomposed products start to accumulate at the interface and participate in internal reactions with transition metal ions and active specifies of the cathode to reduce the practical capacity.[33] Moreover, it was reported that the decomposition of $NaPF_6$ in the electrolyte near the high voltage of 4.3 V can produce the hazardous byproducts such as PF_5 and HF.[34] Therefore, we supposed that the cycle performance can be degraded after several hundred cycles despite the well-retained crystal structure and morphology of the cathode materials. The effective approach to solve this cycle performance problem is to form a stable cathode electrode interphase (CEI) layer directly on the cathode material.[35,36] Moreover, we performed the full-cell tests using Na_2TiFeF_7 (cathode) and hard carbon (anode). To eliminate the irreversible capacity of the hard carbon, the hard carbon anode was precycled in the voltage range of 0.01–2.0 V (vs Na^+/Na). It was confirmed that the specific capacity of the Na_2TiFeF_7‖hard carbon full-cell was ≈177 mAh g^{-1} at ≈10 mA g^{-1} in the range of 1.4-4.2 V (Figure S6a, Supporting Information). Even at 5C, the full-cell delivered the large capacity of ≈125 mAh g^{-1} corresponding to 71% of the capacity at ≈945 mA g^{-1}, which indicates the excellent power-capability. Moreover, it was verified that the Na_2TiFeF_7‖hard carbon full-cell exhibited the outstanding cyclability with the capacity retention of ≈81% with a high coulombic efficiency of above 99% for 300 cycles at ≈189 mA g^{-1} (Figure S6b, Supporting Information). In addition, the electrochemical properties of Na_2TiFeF_7 were compared with those of other cathode materials for SIBs (Figure 3d–e and Figure S7, Supporting Information). It exhibits the most superior energy density among the layered-type, polyanion-type, and Prussian-blue-type materials by delivering ≈623 Wh kg^{-1} at a power density of 31 W kg^{-1}.[37–45] These results indicate the outstanding energy density, power-capability, and stable cycle performance of Na_2TiFeF_7 cathode materials compared to those of other cathode materials for SIBs. In addition, to confirm the contribution of pseudo capacitance, we performed the CV analyses at various scan rates (Figure S8a, Supporting Information). It was verified that the redox reactions of Ti^{3+}/Ti^{4+} and Fe^{2+}/Fe^{3+} are occurred at ≈2.8 and 3.75 V, respectively. The currents of the cathodic and anodic peaks are gradually shifted with increase of the scan rate from 0.2 to 1.0 mV s^{-1}. It was verified that the electrochemical reactions of Na_2TiFeF_7 are primarily based on the bulk-diffusion-controlled reaction ($b \approx 0.56$ in the equation of $i_p = av^b$) (Figure S8b–c, Supporting Information).[46] In addition, we calculated the contribution of pseudo capacitance through the equation of $i(V) = k_1v + k_2v^{1/2}$.[47] Figure S8d (Supporting Information) shows that the contribution of pseudo capacitance in Na_2TiFeF_7 was just ≈19.3% at the scan rate of 1 mV s^{-1} during the charge/discharge, which also supports that overall capacity of Na_2TiFeF_7 is determined by bulk-diffusion-controlled reaction.

2.4. Redox Reaction and Local Structure Evolution in Na_2TiFeF_7

The theoretically expected redox reaction of Na_2TiFeF_7 was investigated using X-ray absorption spectroscopy (XAS) through analysis of both the electronic structure and evolution of the local bonding environment around Ti and Fe. As shown in **Figure 4**a–b, both the Ti K-edge and Fe K-edge spectra reversibly shifted to higher-energy levels during the charge and then returned to the original oxidation state during the discharge. By comparing the reference spectra, ex situ X-ray absorption near-edge structure (XANES) spectra as a function of the cutoff voltage during charge and discharge showed both reversible Ti^{3+}/Ti^{4+} and Fe^{2+}/Fe^{3+} redox reaction during Na^+ de/intercalation in Na_xTiFeF_7. In particular, it was observed that the Ti^{3+}/Ti^{4+} redox reaction mainly occurred in the range from 1.5 to 2.8 V (vs Na^+/Na), whereas the Fe^{2+}/Fe^{3+} redox reaction mainly participated in the range from 3.5 to 4.3 V (vs Na^+/Na). It was also verified that the Ti^{3+}/Ti^{4+} and Fe^{2+}/Fe^{3+} redox reactions in Na_2TiFeF_7 are occurred at ≈2.8 and ≈3.75 V (vs Na^+/Na), respectively, through the cyclic voltammetry (CV) analyses (Figure S9, Supporting Information). These results are consistent with the first-principles calculation results confirmed by the integration of the total number of electron spins.

As the redox reactions of Ti^{3+}/Ti^{4+} and Fe^{2+}/Fe^{3+} occur during Na^+ de/intercalation, the local structure changes of the first neighbor around the transition-metal ion were observed using the ex situ EXAFS analysis (Figure 4c–d). The first neighboring peak around the Ti ion indicating Ti–F bonding was shortened from 1.53 to 1.41 Å as the charging proceeded until 3.5 V, and the bonding distance was maintained during further charge over 3.5 V. In addition, the Fe–F bonding distance was shortened from 1.54 to 1.47 Å as the charging proceeded after 3.5 V. This trend is consistent with the first-principles calculation that the bond distance of Ti–F and Fe–F in TiF_6 and FeF_6 octahedra decreased from ≈2.03 to ≈1.92 Å and from ≈2.08 to ≈1.95 Å, respectively, as the oxidation occurred (Figure 4e). These changes are due to the increased coulombic attraction force between the transition-metal ion and the fluoride ion as the oxidation occurs.

2.5. Structural Change and Reaction Mechanism of Na_2TiFeF_7

To investigate the structure change of Na_2TiFeF_7 during Na^+ de/intercalation, *operando* synchrotron XRD (o-SXRD) analyses were performed (**Figure 5**a and Figure S10, Supporting Information). A monotonous single-phase reaction was observed only accompanied by a change of lattice parameters without phase transition during the charge/discharge. The XRD peaks of Na_2TiFeF_7 corresponding to the (003) and (202) planes were reversibly shifted toward higher/lower 2θ during Na^+ de/intercalation, respectively (Figure 5b and Figure S11, Supporting Information). Through the Rietveld refinement of the o-SXRD patterns, we quantitatively analyzed the reversible change in the lattice parameters and crystal volume during Na^+ de/intercalation (Figure 5c). As the Na^+ ions deintercalated from Na_2TiFeF_7 to Na_0TiFeF_7, the lattice parameters a and c decreased from 7.421 to 7.401 Å and 18.288 to 18.211 Å, respectively, resulting in a decrease of the lattice volume from 872.3 to 863.9 Å³. The total volume change of Na_2TiFeF_7 during Na^+ de/intercalation was verified to be less than ≈0.96% despite the large ionic radius of Na^+ (≈1.02 Å). This volume change is conspicuously small compared with that of layered-type, polyanion, and other SIB cathode materials during Na^+ de/intercalation given that the
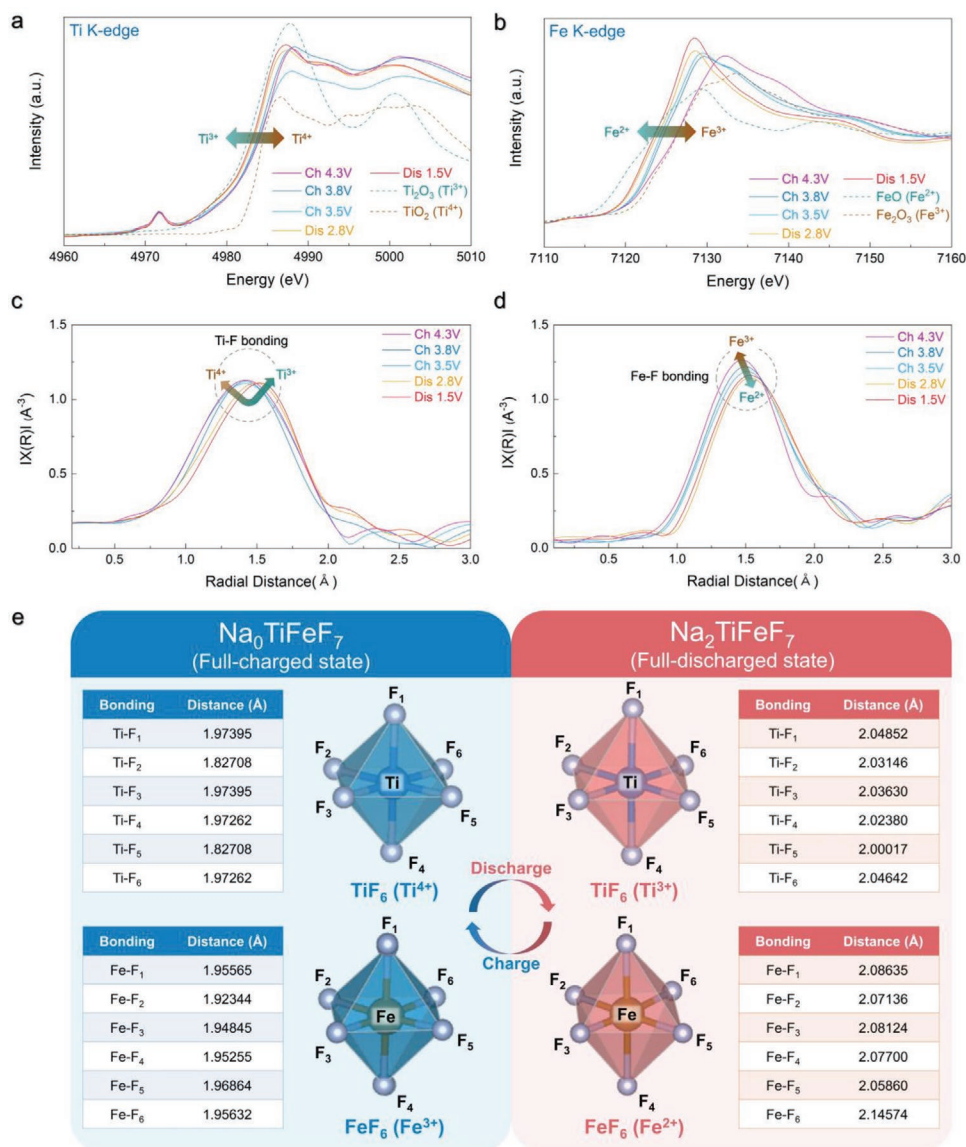
Figure 4. Redox reaction and local structure evolution in Na_2TiFeF_7 during the charge and discharge. Ex situ a) Ti and b) Fe K-edge XANES analyses of Na_xTiFeF_7 ($0 \leq x \leq 2$). Ex situ EXAFS analyses of Na_xTiFeF_7 ($0 \leq x \leq 2$) with the c) Ti–F bonding distance and d) Fe–F bonding distance. e) Comparison of predicted Ti–F and Fe–F bond distance of TiF_6 and FeF_6 octahedra between Na_0TiFeF_7 and Na_2TiFeF_7 determined through the first-principles calculation.

volume change for most cathodes for SIB is in the range of ≈5 to 20%.[48,49] Moreover, we investigated the detailed structural information of fully charged Na_0TiFeF_7 and 1-cycled Na_2TiFeF_7 phases using the Rietveld refinement. As shown in Figures S12–S13 and Tables S3–S4 (Supporting Information), it was clearly confirmed that the crystal structure of Na_2TiFeF_7 was stably retained without any severe structural degradation during Na^+ de/intercalation. In addition, the crystal structure and morphology changes of Na_2TiFeF_7 were investigated using ex situ SEM, TEM, and XRD analyses after numerous charge/discharge cycles (Figure S14, Supporting Information). Compared with the as-prepared electrode, there were no noticeable differences in the crystal structure or morphology even after 600 cycles owing to the small volume change of below ≈0.96%.

A negligible change in lattice parameters and volume was found to be effective in mitigating the internal strain. The lattice strain was calculated using the Williamson–Hall isotropic strain model (W–H ISM)[50,51] based on the o-SXRD patterns, as previously studied using the same procedure.[20] As shown in Figures S15–S16 (Supporting Information), the slope of Na_xTiFeF_7 ($0 \leq x \leq 2$), reflective of the lattice strain, negligibly increased from 0.00462 to 0.00493 (0.031%) during Na^+ deintercalation (from $x = 2$ to $x = 0$). Furthermore, it was reversibly recovered to 0.00469 (0.024%) after Na^+ intercalation (Figure S17, Supporting Information); moreover, the value was much less changed compared with $Na_2Fe_2F_7$ (≈0.249%). The negligible change in the lattice strain of Na_xTiFeF_7 ($0 \leq x \leq 2$) was due to the small volume change during the reversible Na^+ de/intercalation. This result strongly suggests
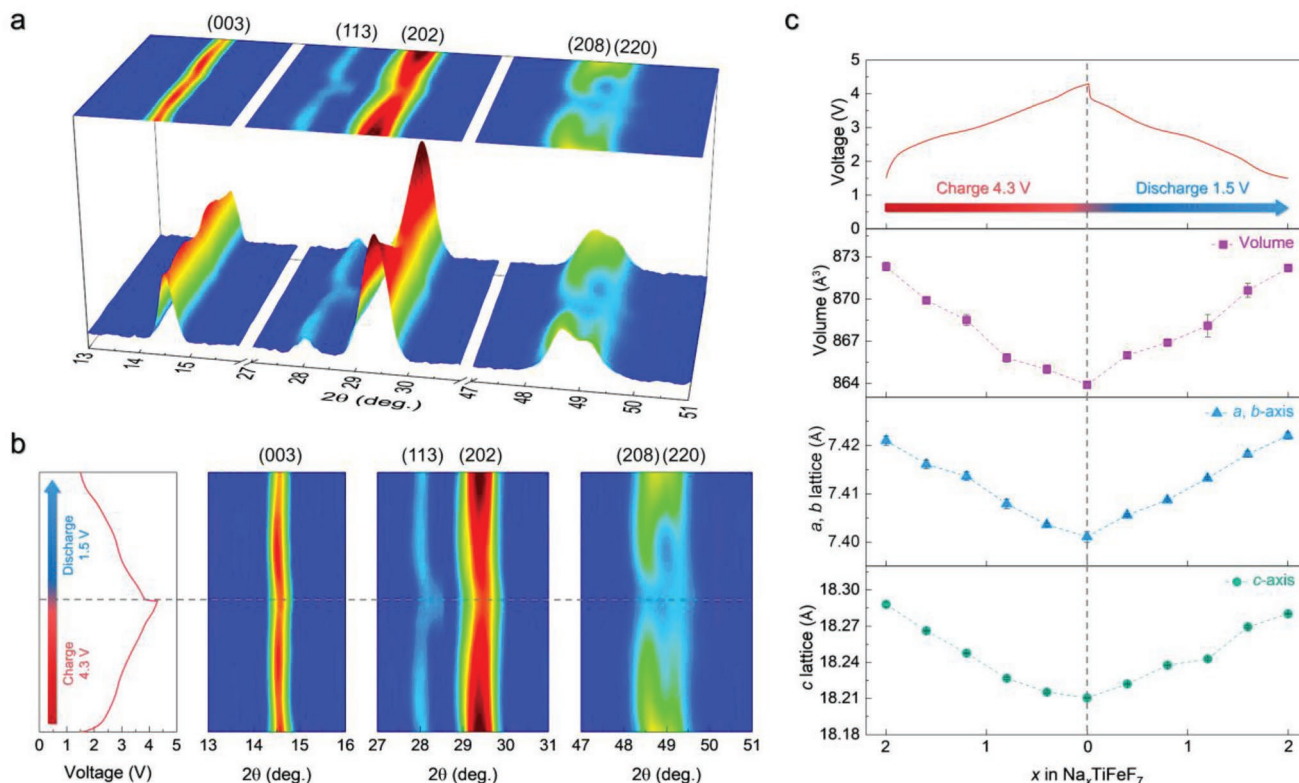
**ADVANCED
SCIENCE NEWS**
www.advancedsciencenews.com

**ADVANCED
FUNCTIONAL
MATERIALS**
www.afm-journal.de

Figure 5. Structural changes and reaction mechanism of Na_2TiFeF_7. a) o-SXRD patterns of Na_xTiFeF_7 ($0 \leq x \leq 2$) measured at a current rate of C/7 in the voltage range of 1.5–4.3 V (vs Na^+/Na). b) Magnified view of o-SXRD patterns with charge/discharge curves of Na_xTiFeF_7 ($0 \leq x \leq 2$). c) Change in lattice parameters a, b, c, and volume of Na_xTiFeF_7 during Na^+ de/intercalation in the structure.

that the Na_2TiFeF_7 cathode will be advantageous for long-term cycle stability in terms of mitigating the crack formation that can cause side reactions or transition-metal dissolution under additional electrolyte exposure.

3. Conclusion

We investigated Na_2TiFeF_7 as a novel fluoride-based cathode material for SIBs with combined analyses using first-principles calculation and various experimental techniques. The presence of Fe^{2+} and Ti^{3+} ions in the structure of Na_2TiFeF_7 also enabled reversible de/intercalation of ≈1.95 mol Na^+ through both redox reactions of Ti^{3+}/Ti^{4+} and Fe^{2+}/Fe^{3+}, which correspond to a specific capacity of ≈185 mAh g^{-1} at C/20 (1C = 189 mA g^{-1}). Moreover, Na_2TiFeF_7 theoretically exhibits the highest Fe^{2+}/Fe^{3+} redox potential of 3.75 V (vs Na^+/Na), which results in a high average operation voltage of ≈3.37 V. In particular, the large three-dimensional pathways for facile Na^+ diffusion, low activation energy barriers (≈477.68 meV), and low band-gap energy (≈1.83 eV) lead to the excellent power-capability of Na_2TiFeF_7, despite the fluoride-based composition. Even at 5C, the specific capacity of Na_2TiFeF_7 was retained up to ≈73% of the theoretical capacity. Furthermore, three-dimensionally interconnected (Fe, Ti)F_6 octahedra can result in a highly stable crystal structure of Na_2TiFeF_7, leading to a small volume change (≈0.96%) during

Na^+ de/intercalation. Thus, Na_2TiFeF_7 can deliver long-term cycle performance with a capacity retention of ≈71% for 600 cycles at 1C with a high coulombic efficiency of above 99%. Our findings will help pave the way for the development of novel, low-cost, fluoride-based cathode materials with outstanding electrochemical properties for SIBs and other alkali-ion batteries.

4. Experimental Section

Synthesis of Na_2TiFeF_7: To prepare the Na_2TiFeF_7 powder, NaF (Alfa Aesar, 99%), TiF_3 (Sigma Aldrich, 99%), and FeF_2 (Alfa Aesar, 98%) in a molar ratio of 2:1:1 were used as precursors. The precursors were sealed in a silicon-nitride jar in an Ar-filled glove box and mixed using high-energy ball-milling at 400 rpm for 12 h. The mixture was pelletized and sintered at 600°C for 30 min under Ar flow. After the calcination, the powder was high-energy ball-milled with 10 wt% pyromellitic acid (PA, $C_6H_{10}O_2$) (Alfa Aesar, 96%). The Na_2TiFeF_7, Super P carbon black, and multiwalled carbon nanotubes (MWCNTs) were homogeneously mixed in a molar ratio of 85:13:2 using high-energy ball milling at 150 rpm for 12 h to improve the electrical conductivity. The carbon-coated sample contained approximately 20 wt% carbon, as confirmed by the thermogravimetric analysis (TGA) (Figure S18, Supporting Information). In addition, the surface areas of the carbon-mixed Na_2TiFeF_7 (Na_2TiFeF_7/C) were measured using the Brunauer-Emmett-Teller (BET) surface area analysis. Figure S19 (Supporting Information) exhibited that the surface area of Na_2TiFeF_7/C was ≈2.5384 m^2 g^{-1}.

Materials Characterization: The crystal structure of Na_2TiFeF_7 was analyzed using X-ray diffraction (XRD) (PANalytical, Empyrean) with Cu Kα radiation (λ = 1.54178 Å). The step size was 0.13°, and the 2θ range was 10°–80°. The Rietveld refinement of the XRD data was performed using the FullProf software. TGA was performed under an Ar atmosphere at a heating rate of 10°C min^{-1} using a thermogravimetric analyzer (Discovery TGA, USA) to 600°C. The atomic ratios of elements such as Na, Ti, and Fe were analyzed using inductively coupled plasma-atomic emission spectroscopy (ICP-AES) at the National Center for Inter-university Research Facilities (NCIRF) at Seoul National University. The Brunauer-Emmett-Teller (BET) (ASAP2460M, USA) method was performed to calculate the specific surface area. The valence states of Ti and Fe in the structure of Na_2TiFeF_7 were determined from the X-ray absorption near-edge structure (XANES) analysis performed at beamline 6D at the Pohang Accelerator Laboratory (PAL), South Korea. Ti K-edge and Fe K-edge spectra were collected in transmission mode with an electron energy of 2.5 GeV and a beam current of 200 mA. Ti and Fe reference spectra were simultaneously obtained from Ti and Fe metal foil. Measurements of the particle size and distribution were performed using scanning electron microscopy (SEM; Hitachi S-4700) and high-resolution transmission electron microscopy (TEM; JEM-3100). *Operando* synchrotron XRD (*o*-SXRD) patterns of Na_2TiFeF_7 were obtained at beamline 3D XRS at PAL, South Korea, using synchrotron radiation (λ = 0.687628 Å) with a Mar345 image plate detector in transmission mode and an X-ray exposure time of 5 s. In addition, the *o*-SXRD patterns were measured during the charge/discharge at a current density of 27 mA g^{-1} within the voltage range of 1.5–4.3 V (vs Na$^+$/Na). After the measurement, the 2θ angles of all the o-SXRD patterns were converted into the corresponding angles λ = 1.54178 Å with Cu Kα radiation for each of comparison with other studies.

Electrochemical Characterization: All data of the specific capacities in the manuscript were calculated based on the 70 wt% active material (Na_2TiFeF_7) in the electrode. The Na_2TiFeF_7 electrode was prepared by mixing 87.5 wt% of the Na_2TiFeF_7/C (80 wt% Na_2TiFeF_7 and 20 wt% conductive carbon), 2.5 wt% Super P carbon black, and 10 wt% PVDF binder using N-methyl-2-pyrrolidone (NMP) as the solvent. Thus, the electrode was composed of 70 wt% Na_2TiFeF_7, 20 wt% conductive carbons, and 10 wt% PVDF binder. The slurry was applied on Al foil using a doctor blade and dried at 100°C for 24 h in a vacuum oven. CR2032-type coin cells were assembled in an Ar-filled glove box using the Na_2TiFeF_7 electrode, Na metal as the counter electrode, a separator (Whatman GF/F glass fiber), and an electrolyte (1.0 M NaPF$_6$ in propylene carbonate (PC) and fluoroethylene carbonate (FEC) in a volume ratio of 98:2). To prevent the undesirable oxidation, the storage of Na_2TiFeF_7 powders and the fabrication of the electrode and the coin-cells were performed in a glove box in an Ar-filled atmosphere (H_2O and O_2 contents of < 0.1 ppm). Moreover, all characterization tests were based on the vacuum-packaging-based transfer process for minimization of exposure to air and moisture. Galvanostatic charge/discharge tests were performed at various C-rates (C/20, C/10, C/5, C/2, 1C, 2C, and 5C in the range of 1.5–4.3 V) using an automatic battery charge/discharge test system (WBCS 3000, WonATech). To measure the electronic conductivity of Na_2TiFeF_7, both sides of the pellet were sputtered with platinum (Pt) as the blocking electrode. To reinforce adhesion between Na_2TiFeF_7 and Pt, the deposited pellet was heated to 120°C in a glovebox. The DC polarization was conducted with an applied voltage of 1.0 V for 3000 s.

Computational Details: All the density functional theory (DFT) calculations were performed using the Vienna Ab initio Simulation Package (VASP).[52] Projector-augmented wave (PAW) pseudopotentials[53] were used with a plane-wave basis set as implemented in VASP. Perdew–Burke–Ernzerhof (PBE) parametrization of the generalized gradient approximation (GGA)[54] was used for the exchange-correlation functional. For the DFT calculations, a $4 \times 4 \times 2$ k-point grid was used to calculate a $1 \times 1 \times 1$ supercell structure of Na_2TiFeF_7. The GGA+U[55] method was adopted to address the localization of the d-orbital in Ti and Fe ions, with U_{eff} values of 2.4 and 5.0 eV, respectively, as used in the previous studies.[56,57] A kinetic energy cutoff of 500 eV was used in all the calculations, and all the structures were optimized until the force in the unit cell converged to within 0.03 eV Å^{-1}. The Cluster-assisted statistical mechanics (CASM) software[58] was used to generate all the Na$^+$/vacancy configurations for each composition, followed by full DFT calculations on a maximum of 20 configurations with the lowest electrostatic energy for each composition used to obtain the convex hull of Na_2TiFeF_7. Nudged elastic band (NEB) calculations[59] were performed to determine the activation barrier for Na$^+$ diffusion in the Na_2TiFeF_7 structure. To perform the calculations, five intermediate images were generated between each Na site. These structures were then calculated using a NEB algorithm with the fixed lattice parameters and free internal atomic positions.

Supporting Information

Supporting Information is available from the Wiley Online Library or from the author.

Conflict of Interest

The authors declare no conflict of interest.

Data Availability Statement

The data that support the findings of this study are available from the corresponding author upon reasonable request.

[1] S. Akhtar, W. Lee, M. Kim, M.-S. Park, W.-S. Yoon, *J. Electrochem. Sci. Technol.* **2021**, *12*, 1.

[2] T. Kim, W. Choi, H.-C. Shin, J.-Y. Choi, J. M. Kim, M.-S. Park, W.-S. Yoon, *J. Electrochem. Sci. Technol.* **2020**, *11*, 14.

[3] C.-Y. Yu, J.-S. Park, H.-G. Jung, K.-Y. Chung, D. Aurbach, Y.-K. Sun, S.-T. Myung, *Energy Environ. Sci.* **2015**, *8*, 2019.

[4] A. Caballero, L. Hernán, J. Morales, L. Sánchez, J. S. Peña, M. A. G. Aranda, *J. Mater. Chem.* **2002**, *12*, 1142.

[5] J. Billaud, R. J. Clement, A. R. Armstrong, J. Canales-Vazquez, P. Rozier, C. P. Grey, P. G. Bruce, *J. Am. Chem. Soc.* **2014**, *136*, 17243.

[6] Y. Gao, Z. Wang, G. Lu, *J. Mater. Chem. A* **2019**, *7*, 2619.

[7] C. Delmas, J.-J. Braconnier, P. Hagenmuller, *Mater. Res. Bull.* **1982**, *17*, 117.

ADVANCED
SCIENCE NEWS

www.advancedsciencenews.com

ADVANCED
FUNCTIONAL
MATERIALS

www.afm-journal.de

[8] Z.-Y. Li, R. Gao, J. Zhang, X. Zhang, Z. Hu, X. Liu, *J. Mater. Chem. A* **2016**, *4*, 3453.

[9] I. Lee, G. Oh, S. Lee, T.-Y. Yu, M. H. Alfaruqi, V. Mathew, B. Sambandam, Y.-K. Sun, J.-Y. Hwang, J. Kim, *Energy Storage Mater.* **2021**, *41*, 183.

[10] Q. Wang, E. Hu, Y. Pan, N. Xiao, F. Hong, Z. Fu, X. Wu, S. Bak, X. Yang, Y. Zhou, *Adv. Sci.* **2017**, *4*, 1700219.

[11] N. Yabuuchi, H. Yoshida, S. Komaba, *Electrochemistry* **2012**, *80*, 716.

[12] E. Lee, D. E. Brown, E. E. Alp, Y. Ren, J. Lu, J.-J. Woo, C. S. Johnson, *Chem. Mater.* **2015**, *27*, 6755.

[13] C. Ding, T. Nohira, R. Hagiwara, *Electrochim. Acta* **2017**, *231*, 412.

[14] J. U. Choi, Y. J. Park, J. H. Jo, L.-Y. Kuo, P. Kaghazchi, S.-T. Myung, *ACS Appl. Mater. Interfaces* **2018**, *10*, 40978.

[15] W. Ko, J.-K. Yoo, H. Park, Y. Lee, I. Kang, J. Kang, J. H. Jo, J. U. Choi, J. Hong, S.-T. Myung, J. Kim, *Nano Energy* **2020**, *77*, 105175.

[16] J. Kim, H. Kim, I. Park, Y.-U. Park, J.-K. Yoo, K.-Y. Park, S. Lee, K. Kang, *Energy Environ. Sci.* **2013**, *6*, 830.

[17] S.-W. Kim, D.-H. Seo, H. Kim, K.-Y. Park, K. Kang, *Phys. Chem. Chem. Phys.* **2012**, *14*, 3299.

[18] H. Park, J.-K. Yoo, W. Ko, Y. Lee, I. Park, S.-T. Myung, J. Kim, *J. Power Sources* **2019**, *434*, 226750.

[19] G. Ali, S. H. Oh, S. Y. Kim, J. Y. Kim, B. W. Cho, K. Y. Chung, *J. Mater. Chem. A* **2015**, *3*, 10258.

[20] H. Park, Y. Lee, M. Cho, J. Kang, W. Ko, Y. H. Jung, T. Jeon, J. Hong, H. Kim, S.-T. Myung, J. Kim, *Energy Environ. Sci.* **2021**, *14*, 1469.

[21] K. V. Kravchyk, T. Zünd, M. Wörle, M. V. Kovalenko, M. I. Bodnarchuk, *Chem. Mater.* **2018**, *30*, 1825.

[22] I. Hwang, S.-K. Jung, E.-S. Jeong, H. Kim, S.-P. Cho, K. Ku, H. Kim, W.-S. Yoon, K. Kang, *Nano Res.* **2017**, *10*, 4388.

[23] S. Wei, X. Wang, M. Liu, R. Zhang, G. Wang, H. Hu, *J. Energy Chem.* **2018**, *27*, 573.

[24] T. Yi, W. Chen, L. Cheng, R. D. Bayliss, F. Lin, M. R. Plews, D. Nordlund, M. M. Doeff, K. A. Persson, J. Cabana, *Chem. Mater.* **2017**, *29*, 1561.

[25] M. Jiang, X. Wang, Y. Shen, H. Hu, Y. Fu, X. Yang, *Electrochim. Acta* **2015**, *186*, 7.

[26] Y. Yamada, T. Doi, I. Tanaka, S. Okada, J. Yamaki, *J. Power Sources* **2011**, *196*, 4837.

[27] W. Ko, M.-K. Cho, J. Kang, H. Park, J. Ahn, Y. Lee, S. Lee, S. Lee, K. Heo, J. Hong, J.-K. Yoo, J. Kim, *Energy Storage Mater.* **2022**, *46*, 289.

[28] I. D. Brown, D. Altermatt, *Acta Crystallogr. Sect. B Struct. Sci.* **1985**, *41*, 244.

[29] P. Barpanda, G. Oyama, S. Nishimura, S.-C. Chung, A. Yamada, *Nat. Commun.* **2014**, *5*, 4358.

[30] K. Lee, S. Han, J. Lee, S. Lee, J. Kim, Y. Ko, S. Kim, K. Yoon, J.-H. Song, J. H. Noh, K. Kang, *ACS Energy Lett.* **2022**, *7*, 381.

[31] S. K. Jung, H. Gwon, G. Yoon, L. J. Miara, V. Lacivita, J. S. Kim, *ACS Energy Lett.* **2021**, *6*, 2006.

[32] I. Moeez, D. Susanto, W. Chang, H.-D. Lim, K. Y. Chung, *Chem. Eng. J.* **2021**, *425*, 130547.

[33] S. Guo, Q. Li, P. Liu, M. Chen, H. Zhou, *Nat. Commun.* **2017**, *8*, 135.

[34] S. Liu, L. Wang, C. Zhang, B. Chu, C. Wang, T. Huang, A. Yu, *J. Power Sources* **2019**, *438*, 226979.

[35] L. Fan, Y. Hu, A. M. Rao, J. Zhou, Z. Hou, C. Wang, B. Lu, *Small Methods* **2021**, *5*, 2101131.

[36] Z. Liu, Y. Yang, S. Liang, B. Lu, J. Zhou, *Small Struct* **2021**, *2*, 2100119.

[37] X. Li, T. Wang, Y. Yuan, X. Yue, Q. Wang, J. Wang, J. Zhong, R. Lin, Y. Yao, X. Wu, X. Yu, Z. Fu, Y. Xia, X. Yang, T. Liu, K. Amine, Z. Shadike, Y. Zhou, J. Lu, *Adv. Mater.* **2021**, *33*, 2008194.

[38] C. Zhou, L. Yang, C. Zhou, B. Lu, J. Liu, L. Ouyang, R. Hu, J. Liu, M. Zhu, *ACS Appl. Mater. Interfaces* **2019**, *11*, 7906.

[39] D. Yuan, X. Liang, L. Wu, Y. Cao, X. Ai, J. Feng, H. Yang, *Adv. Mater.* **2014**, *26*, 6301.

[40] J. E. Wang, W. H. Han, K. J. Chang, Y. H. Jung, D. K. Kim, *J. Mater. Chem. A* **2018**, *6*, 22731.

[41] T. Hwang, J.-H. Lee, S. H. Choi, R.-G. Oh, D. Kim, M. Cho, W. Cho, M.-S. Park, *ACS Appl. Mater. Interfaces* **2019**, *11*, 30894.

[42] H. Kim, G. Yoon, I. Park, K. Y. Park, B. Lee, J. Kim, Y. U. Park, S. K. Jung, H. D. Lim, D. Ahn, S. Lee, K. Kang, *Energy Environ. Sci.* **2015**, *8*, 3325.

[43] W. Zhang, H. Li, Z. Zhang, M. Xu, Y. Lai, S. Chou, *Small* **2020**, *16*, 2001524.

[44] Y. Zhou, X. Shao, K. Lam, Y. Zheng, L. Zhao, K. Wang, J. Zhao, F. Chen, X. Hou, *ACS Appl. Mater. Interfaces* **2020**, *12*, 30328.

[45] Y. Liu, Y. Qiao, W. Zhang, Z. Li, X. Ji, L. Miao, L. Yuan, X. Hu, Y. Huang, *Nano Energy* **2015**, *12*, 386.

[46] V. Augustyn, J. Come, M. A. Lowe, J. W. Kim, P.-L. Taberna, S. H. Tolbert, H. D. Abruña, P. Simon, B. Dunn, *Nat. Mater.* **2013**, *12*, 518.

[47] J. Wang, J. Polleux, J. Lim, B. Dunn, *J. Phys. Chem. C* **2007**, *111*, 14925.

[48] Z. Lu, J. R. Dahn, *J. Electrochem. Soc.* **2001**, *148*, A1225.

[49] J. Kang, H. Park, H. Kim, J. H. Jo, W. Ko, Y. Lee, S. Myung, J. Kim, *ACS Sustainable Chem. Eng.* **2020**, *8*, 163.

[50] P. M. Shafi, A. C. Bose, *AIP Adv.* **2015**, *5*, 057137.

[51] K. Venkateswarlu, A. C. Bose, N. Rameshbabu, *Phys. B Condens. Matter* **2010**, *405*, 4256.

[52] G. Kresse, J. Furthmüller, *Comput. Mater. Sci.* **1996**, *6*, 15.

[53] P. E. Blöchl, *Phys. Rev. B* **1994**, *50*, 17953.

[54] J. P. Perdew, K. Burke, M. Ernzerhof, *Phys. Rev. Lett.* **1996**, *77*, 3865.

[55] V. I. Anisimov, F. Aryasetiawan, A. I. Lichtenstein, *J. Phys. Condens. Matter* **1997**, *9*, 767.

[56] Z. Li, B. Wang, C. Li, J. Liu, W. Zhang, *J. Mater. Chem. A* **2015**, *3*, 16222.

[57] R. Shirakami, H. Ueda, H. O. Jeschke, H. Nakano, S. Kobayashi, A. Matsuo, T. Sakai, N. Katayama, H. Sawa, K. Kindo, C. Michioka, K. Yoshimura, *Phys. Rev. B* **2019**, *100*, 174401.

[58] A. Van der Ven, J. C. Thomas, Q. Xu, J. Bhattacharya, *Math. Comput. Simul.* **2010**, *80*, 1393.

[59] G. Henkelman, B. P. Uberuaga, H. Jónsson, *J. Chem. Phys.* **2000**, *113*, 9901.